coatings

MDPI

*Article*

# Role of the Alkylation Patterning in the Performance of OTFTs: The Case of Thiophene-Functionalized Triindoles

**Roger Bujaldón [1,2,†], Alba Cuadrado [1,2,†], Dmytro Volyniuk [3], Juozas V. Grazulevicius [3], Joaquim Puigdollers [4] and Dolores Velasco [1,2,*]**

[1] Grup de Materials Orgànics, Departament de Química Inorgànica i Orgànica, Secció de Química Orgànica, Universitat de Barcelona, Martí i Franquès, 1, E-08028 Barcelona, Spain; rr.bujaldon@ub.edu (R.B.); a.cuadradosantolaria@gmail.com (A.C.)
[2] Institut de Nanociència i Nanotecnologia (IN2UB), Universitat de Barcelona, E-08028 Barcelona, Spain
[3] Department of Polymer Chemistry and Technology, Kaunas University of Technology, Radvilenu pl. 19, LT-50254 Kaunas, Lithuania; juozas.grazulevicius@ktu.lt (J.V.G.)
[4] Departament d'Enginyeria Electrònica, Universitat Politècnica de Catalunya, Jordi Girona, 1–3, E-08034 Barcelona, Spain; joaquim.puigdollers@upc.edu
* Correspondence: dvelasco@ub.edu
† These authors contributed equally to this work.

**Abstract:** Organic semiconductors have emerged as potential alternatives to conventional inorganic materials due to their numerous assets and applications. In this context, the star-shaped triindole core stands as a promising system to design new organic materials with enticing charge-transporting properties. Herein, we present the synthesis of three thiophene-containing triindole derivatives that feature *N*-alkyl chains of different lengths, from methyl to decyl. The impact of the alkylation patterning on the crystallinity of the thin films and their resultant performance as semiconductor have been analyzed. All derivatives displayed p-type semiconductor properties, as demonstrated via both TOF measurements and integration in organic thin-film transistor (OTFT) devices. The attachment of longer alkyl chains and the functionalization of the silicon substrate with octadecyltrichlorosilane (OTS) prompted better OTFT characteristics, with a hole mobility value up to $5 \times 10^{-4}$ $cm^2$ $V^{-1}$ $s^{-1}$. As elucidated from the single crystal, this core is arranged in a convenient cofacial packing that maximizes the π-overlapping. The analysis of the thin films also corroborates that derivatives possessing longer *N*-alkyl chains confer a higher degree of order and a more adequate morphology.

**Keywords:** alkylation patterning; carbazole; organic chemistry; organic semiconductors; OTFTs; triindole; thin-film morphology



**Citation:** Bujaldón, R.; Cuadrado, A.; Volyniuk, D.; Grazulevicius, J.V.; Puigdollers, J.; Velasco, D. Role of the Alkylation Patterning in the Performance of OTFTs: The Case of Thiophene-Functionalized Triindoles. *Coatings* **2023**, *13*, 896. https://doi.org/10.3390/coatings13050896

Academic Editors: Zohra Benzarti and Ali Khalfallah

Received: 31 March 2023
Revised: 3 May 2023
Accepted: 5 May 2023
Published: 9 May 2023



## 1. Introduction

The current upsurge in organic electronics acknowledges the potential of organic semiconductors as a realistic alternative to conventional inorganic materials [1,2]. Even though the state-of-the-art technology in this area still cannot compete with the performance of crystalline silicon in terms of charge mobility, several materials have already surpassed the milestone of 10 $cm^2$ $V^{-1}$ $s^{-1}$ [3,4]. Furthermore, the aim of organic materials is not substituting inorganic ones in high-performing applications but rather granting desired features in next-generation devices, such as flexibility or transparency. Their many advantages also encompass uses from the fabrication of large-area displays with a lower production cost to the modulation of their properties via facile synthetic methods [2,5–7].

The π-conjugated backbone of an organic compound rules fundamental properties, such as the electronic profile, the arrangement in the solid state, the air stability, and the optical characteristics [8–10]. Since the structural design represents the cornerstone of an organic semiconductor, the investigation of this topic has led to countless molecular structures developed from a wide array of building blocks [3,6,11–15]. Apart from the key

role of the main aromatic nucleus, however, additional structural features can be equally decisive in governing the semiconductor characteristics of a material. A prime example of this is the inclusion of flexible alkyl chains, which not only improve the solubility but also influence the intermolecular interactions in the solid state [16–20]. Therefore, the alkylation patterning in a particular core should be carefully addressed to extract its full potential in terms of charge carrier mobility.

In this way, 9*H*-carbazole emerges as a highly promising nucleus that can supply several characteristics needed in novel materials, e.g., hole-transporting properties with stability against oxidative doping by atmospheric oxygen [13,21] and high fluorescence [22,23]. Additionally, it embeds nitrogen as a heteroatom that provides a suitable point to insert alkyl chains. The case of the diindolo[3,2-*a*:3′,2′-*c*]carbazole core, also known as triindole, represents a particularly enticing system constructed from carbazole that features a star-shaped π-extension [24,25]. The successful integration of triindole-based structures in assorted devices, such as OSCs [26–28], OLEDs [29–31], and, more recently, OTFTs [18,32–34], clearly reinforces their potential.

Herein, we report the synthesis of a set of new triindole derivatives functionalized with thiophene moieties and their integration in OTFT devices. The inclusion of sulfur-containing heterocycles, such as thiophene, represents a well-known strategy in the search for novel materials within organic electronics [35–40]. The advantages of attaching sulfurated moieties, such as 5-methylthien-2-yl and benzothien-2-yl, to the triindole core, instead of aromatic hydrocarbons, have been already demonstrated in our research group [33]. In this particular study, the 3,8,13-tri(thiophen-2-yl)-10,15-dihydro-5*H*-diindolo[3,2-*a*:3′,2′-*c*] carbazole nucleus has been characterized as a p-type semiconductor and structurally ameliorated considering both the molecular and the device design. Synthetically, this core has been *N*-alkylated with chains of different lengths, from methyl to decyl, as shown in Figure 1. Regarding the architecture of the device, the focus has been placed on optimizing the interface between these semiconductors and the $Si/SiO_2$ substrate in a bottom-gate top-contact OTFT. In fact, the presence of a passivation coating or anchored groups in the interface can greatly influence the growth and features of a vacuum-deposited thin film [41–45]. Specifically, the $SiO_2$ surface has been either functionalized with octadecyltrichlorosilane (OTS) as an aliphatic self-assembled monolayer (SAM) or coated with polystyrene (PS) as an aromatic polymeric layer. The effects of both the *N*-alkylation patterning and the passivation layer over the performance of this core have been correlated with the degree of order and morphology of the thin films, confirming the relevance of an adequate structural design.

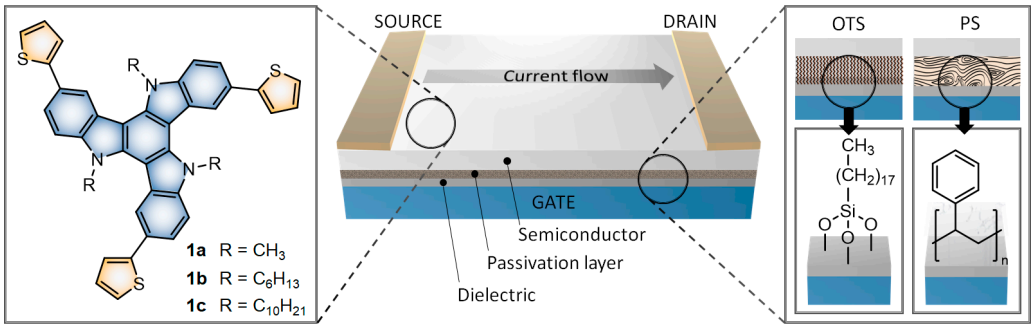


**Figure 1.** Molecular design of the studied thiophene-substituted triindoles **1a–c** and the architecture of the OTFT devices, constructed over $Si/SiO_2$ substrates coated with either OTS or PS.

## 2. Materials and Methods

### *2.1. Synthesis and Characterization*

The commercially available chemicals were employed as received. Chemicals and reagents were as follows: 5-bromoisatin (Alfa Aesar, 91.2%), sodium hydride (Aldrich, 60% dispersion in mineral oil), methyl iodide (Acros Organics, 99%), 1-bromohexane (Aldrich, 98%), 1-bromodecane (Aldrich, 98%), hydrazine hydrate (Sigma-Aldrich, reagent grade,

55% $N_2H_4$), phosphorous(V) oxychloride (Acros Organics, 99%), 2-thienylboronic acid (TCI, 98.7%), and $Pd(PPh_3)_4$ (Acros Organics, 99%). Anhydrous DMF (Thermo Scientific) was kept under nitrogen atmosphere over a molecular sieve. Dichloromethane (VWR) was distilled from $CaH_2$. Flash chromatography was carried out over commercial silica gel (VWR, 40–63 μm). All synthetic procedures were carried out in open-air atmosphere unless otherwise stated.

### *2.2. Instrumentation and Methods*

Here, $^1$H NMR (400 MHz) and $^{13}$C NMR (100 MHz) spectra were collected in a Varian Mercury spectrophotometer (Varian Inc., Palo Alto, CA, USA). In the case of compound **1a**, the $^{13}$C NMR (100 MHz) spectrum was recorded in a Bruker 400 MHz Avance III. The analysis of the NMR spectra was achieved using MestRec Nova software (version 14.2.0). The solvent signal was used to reference all the spectra. Absorption spectra were registered on a Varian Cary UV–Vis–NIR 500E spectrophotometer (Palo Alto, CA, USA) and emission spectra were registered using a PTI fluorimeter (Birmingham, AL, USA). 1,4-Bis(5-phenyl-2-oxazolyl)benzene (POPOP) was selected as the standard ($\lambda_{Ex}$ = 300 nm, $\Phi$ = 0.93 in cyclohexane) for the analysis of the fluorescence quantum yields, as suggested in the literature protocol [46]. Fluorescence quantum yields of thin films were determined by means of an integrating sphere. Cyclic voltammograms were registered in a cylindrical three-electrode cell using the following electrodes: an $Ag/Ag^+$ electrode (1 mM $AgNO_3$ in acetonitrile) as the reference electrode, a glassy-carbon electrode as the working electrode, and a platinum wire as the counter electrode. All voltammetric curves were recorded with a microcomputer-controlled potentiostat/galvanostat Autolab with PGSTAT30 equipment (Metrohm Autolab BV, Utrecht, The Netherlands) and GPES software (version 4.9) under quiescent conditions, at a scan rate of 100 mV $s^{-1}$ and under an argon atmosphere. The solutions were prepared in distilled dichloromethane (1 mM) with tetrabutylammonium hexafluorophosphate (TBAP) as the supporting electrolyte (0.1 M). The potentials were referred to the $Fc^+/Fc$ redox couple. The ionization potentials (IP) were calculated from the onset of the first oxidation peak as IP = $^{ox}E_{onset}$ + 5.39, where 5.39 eV stands as the formal potential of the $Fc^+/Fc$ couple in the Fermi scale [47]. The electron affinities (EA) were estimated as EA = IP − $E_{gap}$. The optical gap energies ($E_{gap}$) were estimated from the absorption spectra ($\lambda_{onset}$). Ionization potentials (IP) in the solid state were measured by the photoelectron emission method in air. Thin films for IP measurements were prepared by vacuum thermal evaporation ($10^{-6}$ mbar) of the organic compounds on glass slides coated with fluorine-doped tin oxide. A negative voltage of 300 V was applied to the sample substrate. A deep UV deuterium light source (ASBN-D130-CM) and a CM110 1/8m monochromator (Spectral Products, Putnam, CT, USA) were used for illumination of the samples with monochromatic light. A 6517B Keithley electrometer (Keithley, Solon, OH, USA) was connected to the counter electrode for the photocurrent measurement, which was flowing in the circuit under illumination. An energy scan of the incident photons was performed while increasing the photon energy. Thermogravimetric analyses (TGA) were recorded at a heating rate of 20 °C $min^{-1}$ under nitrogen atmosphere using a TA Instruments Q50 (New Castle, DE, USA). The extraction of the charge drift mobility was performed by means of the TOF technique. The organic compounds were vacuum-deposited ($10^{-6}$ mbar) on pre-cleaned indium tin oxide (ITO)-coated glass substrates, and then 80 nm of an aluminum layer was also deposited via thermal vacuum evaporation using a mask (area = 0.06 $cm^2$). Photo generation of charge carriers was performed by a light pulse through the ITO. A Keithley 6517B electrometer was used to apply external voltages with a pulsed third-harmonic Nd:YAG laser EKSPLA NL300 (pulse duration of 3–6 ns, $\lambda$ = 355 nm). A Tektronix TDS 3032C digital storage oscilloscope was used to record the TOF transients. The transit times ($t_t$) were calculated using the kink on the curve of the transient in the log–log scale. The drift mobilities were calculated as $\mu = d^2/Ut_t$, where $d$ is the layer thickness and $U$ is the surface potential at the moment of illumination. Zero-field mobilities ($\mu_0$) and field dependence parameters ($\alpha$) were extracted

from $\mu = \mu_0 e^{\alpha E^{1/2}}$. The single crystal was analyzed using a D8 Venture System (Bruker AXS, Karlsruhe, Germany) equipped with a multilayer monochromator and a Mo microfocus (λ = 0.71073 Å). The frames were integrated with the Bruker SAINT software package (version SAINT V8.38A) via a narrow-frame algorithm. The structure was elucidated and refined using the Bruker SHELXTL software package. Out-of-plane GIXRD measurements were performed on vacuum-deposited thin films (semiconductor thickness = 75 nm) with a PANalytical X'Pert PRO MRD diffractometer (Almelo, the Netherlands) possessing a PIXcel detector, a parabolic Göbel mirror at the incident beam, and a parallel plate collimator at the diffracted beam (Cu K$\alpha$ radiation ($\lambda$ = 1.5418 Å), with a work power of 45 kV × 40 mA). The optimized angle of incidence used was 0.20° (**1a**) or 0.18° (**1b,c**). The morphology of the layers, analyzed by means of atomic force microscopy (AFM), was profiled using an AFM Dimension 3100 system connected to a Nanoscope IVa electronics unit (Bruker, Billerica, MA, USA).

### *2.3. OTFT Fabrication and Characterization*

OTFTs were constructed in a bottom-gate top-contact geometry using thermally-oxidized crystalline-silicon wafers with a $SiO_2$ layer as the gate dielectric. The gate side of the substrates was partially unprotected with ammonium fluoride. Then, the wafers were cleansed by subsequent ultrasonic treatments in acetone, isopropyl alcohol, and water, dried by a nitrogen blow, and heated at 100 °C for 5 min. The $SiO_2$ surface was then either functionalized with octadecyltrichlorosilane (OTS) or coated with polystyrene (PS). The functionalization with OTS SAMs [48,49] was achieved by immersing the substrates in a solution of OTS in toluene (2 mM) for 24 h at room temperature. Then, the substrates were cleaned by subsequent ultrasonic treatments in toluene, acetone, and isopropyl alcohol, and finally dried by a nitrogen blow and heated at 100 °C for 5 min. The coating with PS was carried out with a solution of PS in toluene (4 mg $mL^{-1}$), which was spin-coated onto the wafer. The substrate was spun at 1500 rpm for 5 s and 2500 rpm for 33 s with a P6700 spin-coater (Specialty Coating System, Indianapolis, IN, USA). The organic semiconductor was deposited by thermal evaporation in a vacuum system with a base pressure below $10^{-6}$ mbar. The temperature was manually controlled to ensure a stable deposition rate of 0.3 Å $s^{-1}$ until a thickness of ca. 75 nm was obtained. Then, the substrates were transferred to a different vacuum chamber to deposit the metallic contacts. Gold was chosen as the metal for the drain and source electrodes, which were defined with a metallic mask possessing a channel length ($L$) of 80 μm and width ($W$) of 2 mm. The OTFTs were electrically characterized in the dark under ambient conditions using a Keithley 2636A source meter (Solon, OH, USA). The charge carrier mobility was extracted in the saturation regime ($\mu_{sat}$) from Equation (1), as follows:

$$I_D = \frac{W\, C_{ox}\, \mu}{2\, L}(V_G - V_{th})^2 \quad (1)$$

where $W$ and $L$ are the channel width and length, respectively, and $C_{ox}$ is the unit dimensional dielectric capacitance of the gate insulator.

## 3. Results and Discussion

### *3.1. Synthesis and Characterization*

The synthesis towards the final compounds **1a–c**, which started with the commercially available 5-bromoisatin, is presented in Scheme 1. The alkylation of the starting material was conducted under standard conditions, using NaH and $CH_3I$ to obtain **2a** or $K_2CO_3$ and the corresponding 1-bromoalkane in the case of **2b** and **2c**. Then, the reduction via the Wolff–Kishner reaction led to the 5-bromooxindole derivatives **3a–c**. The cyclocondensation towards the brominated triindole systems, accomplished with $POCl_3$ under reflux, prompted a higher yield for the derivatives featuring shorter alkyl chains. Finally, the attachment of the thiophene moieties was achieved through the Suzuki–Miyaura cross-coupling reaction [50]. It should be mentioned that the severe insolubility of the methylated

precursor **4a** required the use of microwave irradiation to provide the desired compound **1a** in a comparable yield.

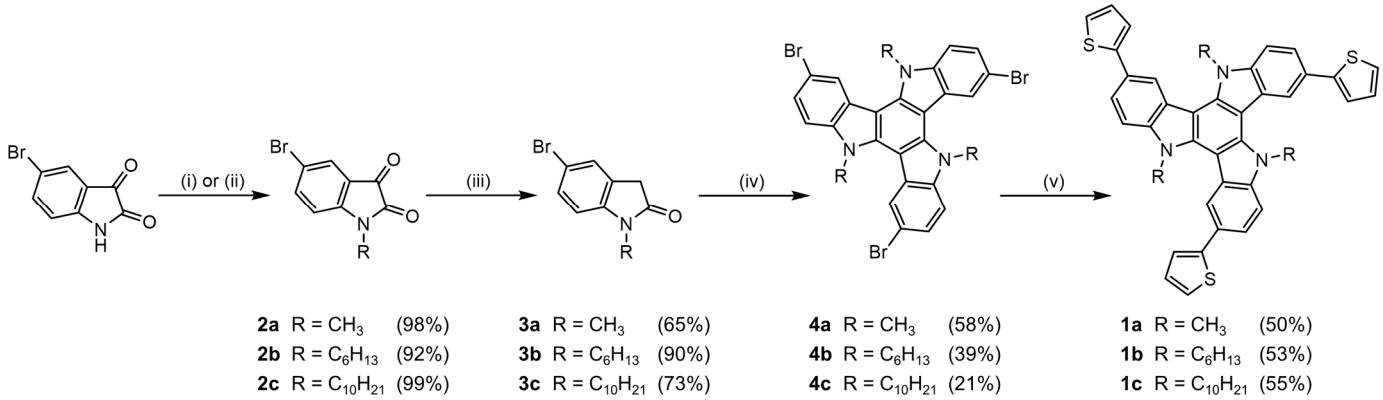


**Scheme 1.** Synthetic route followed to furnish the organic semiconductors **1a–c**. Reagents and conditions: (i) NaH and $CH_3I$ in DMF at RT for the synthesis of **2a** or (ii) $K_2CO_3$ and R-Br in DMF at RT for the synthesis of **2b**,**c**; (iii) $NH_2NH_2{\cdot}H_2O$, reflux; (iv) $POCl_3$, reflux; (v) 2-thienylboronic acid, $Pd(PPh_3)_4$ and $K_2CO_3$ in $THF:H_2O$, μW (**1a**) or reflux (**1b**,**c**).

### *3.2. Physical Characterization*

The thermal and optical properties in solution and in the solid state of compounds **1a–c** are compiled in Table 1. Remarkably, all compounds are suitable for the vacuum-evaporation process, with decomposition temperatures ($T_d$) that surpass 425 °C (TGA scans are depicted in the Supporting Information).

**Table 1.** Thermal and optical properties in solution and in the solid state of derivatives **1a–c**.

| | | Solution [2] | | | Solid State [3] | | |
|---|---|---|---|---|---|---|---|
| **Compound** | $T_d$ (°C) [1] | $\lambda_{abs,max}$ (nm) | $\lambda_{em,max}$ (nm) | $\Phi_f$ [4] | $\lambda_{abs,max}$ (nm) | $\lambda_{em,max}$ (nm) | $\Phi_f$ [4] |
| **1a** | 476 | 317, 344 | 395, 414 | 0.14 | 315, 353 | 432 | 0.02 |
| **1b** | 433 | 318, 344 | 397, 415 | 0.15 | 316, 350 | 424 | 0.03 |
| **1c** | 427 | 318, 344 | 397, 415 | 0.15 | 313, 352 | 424 | 0.03 |

[1] Onset decomposition temperature obtained from TGA. [2] Optical properties determined from a 10 μM solution in $CH_2Cl_2$. [3] Optical properties determined from a vacuum-evaporated thin film of the compound deposited over quartz. [4] Fluorescence quantum yield ($\Phi_f$) obtained with an integration sphere ($\lambda_{ex}$ = 330 nm).

In terms of the optical properties, derivatives **1a–c** display similar characteristics regardless of the length of the *N*-alkyl chains. All of them emit into the UV–blue region, peaking at 415 nm in $CH_2Cl_2$ and displaying a considerable fluorescence quantum yield of ca. 0.15. In the solid state, the emission spectra are slightly red-shifted and broadened, with a decay of the fluorescence quantum yield to ca. 0.03, which is associated to the aggregation of the triindole systems. The absorption and emission spectra of derivatives **1a–c** are represented in the Supporting Information.

The electrochemical properties of **1a–c**, analyzed by means of cyclic voltammetry in $CH_2Cl_2$, are listed in Table 2. All compounds exhibited a first quasi-reversible oxidation process and a second irreversible one, whereas no reduction process could be observed. Consequently, the ionization potentials could be estimated. Their values are slightly conditioned by the length of the *N*-alkyl chains, ranging from 5.58 to 5.66 eV in derivatives **1a** and **1c**, respectively. These values are translated into quite low-lying HOMO energy levels, conferring stability against atmospheric oxygen to the structure while also being suitable for hole injection. The energy of the optical band gaps ($E_{gap}$) was estimated to be 3.22 eV in all three cases, which is smaller than that of the bare triindole system (3.53 eV [20]) because of the more extended π-conjugation of the system. The ionization potentials were also estimated in the solid state though the photoelectron emission technique as a closer

approximation of the device conditions. The featured values, which go from 5.11 eV (**1b**,**c**) to 5.18 eV (**1a**), should ensure an optimal injection process due to the closeness to the gold work function (5.1 eV). The resulting energy levels are represented in Figure 2. The cyclic voltammograms and the photoelectron emission spectra are compiled in the Supporting Information.

**Table 2.** Electrochemical characterization of derivatives **1a–c**.

| Compound | $E_{gap}$ (eV) [1] | $^{ox}E_{onset}$ (V) [2] | IP (eV) [3] | EA (eV) [4] | IP (eV) [5] |
|---|---|---|---|---|---|
| **1a** | 3.22 | 0.18 | 5.58 | 2.36 | 5.18 |
| **1b** | 3.22 | 0.21 | 5.60 | 2.38 | 5.11 |
| **1c** | 3.22 | 0.27 | 5.66 | 2.44 | 5.11 |

[1] Optical energy gap ($E_{gap}$) estimated from the absorption spectrum ($\lambda_{abs,onset}$) in $CH_2Cl_2$. [2] Onset oxidation potential ($^{ox}E_{onset}$) vs. $Fc^+/Fc$ determined from CV in dichloromethane (1 mM). [3] Ionization potential (IP) estimated as IP = $^{ox}E_{onset\ vs.\ Fc+/Fc}$ + 5.39. [4] Electron affinity (EA) estimated as EA = IP − $E_{gap}$. [5] Ionization potential (IP) in the solid state, determined via the photoelectron emission technique.

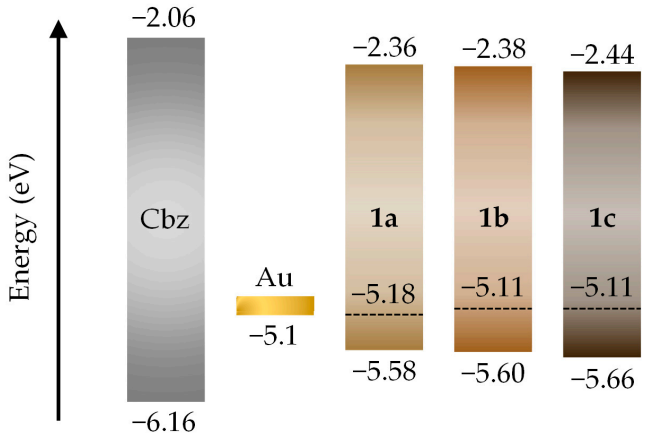


**Figure 2.** Energy levels of 9*H*-carbazole (Cbz) [34] and compounds **1a–c** with respect to the gold work function (the dashed lines correspond to the energy levels calculated from the photoelectron emission technique in the solid state).

The charge-transporting properties of the final compounds **1a–c** were analyzed via the time-of-flight (TOF) technique as a first approximation (Table 3). The graphics containing the TOF transients and the dependence of the hole drift mobilities are collected in the Supporting Information. All three compounds showed a non-dispersive behavior and anticipated promising p-type semiconductor properties. As observed, the extracted mobility values are highly conditioned by the *N*-alkylation patterning. Derivative **1a**, featuring the shortest *N*-alkyl chain, displays a maximum $\mu_h$ of $7 \times 10^{-5}$ $cm^2\ V^{-1}\ s^{-1}$ that is clearly outdone by its analogs **1b,c** ($1 \times 10^{-3}$ $cm^2\ V^{-1}\ s^{-1}$). This enhancement, which goes up to an order of magnitude, manifests the preference of longer *N*-alkyl chains in this particular core. Nevertheless, a further elongation from hexyl to decyl did not show a substantial modification using this technique.

**Table 3.** Charge carrier mobility values of derivatives **1a–c** obtained from TOF measurements.

| Compound | $\mu_h$ ($cm^2\ V^{-1}\ s^{-1}$) [E ($V\ cm^{-1}$)] [1] | $\mu_0$ ($cm^2\ V^{-1}\ s^{-1}$) [2] | $\alpha$ ($(cm\ V^{-1})^{1/2}$) [3] |
|---|---|---|---|
| **1a** | $7 \times 10^{-5}$ [$7 \times 10^5$] | $4 \times 10^{-6}$ | 0.0034 |
| **1b** | $1 \times 10^{-3}$ [$2 \times 10^5$] | $6 \times 10^{-4}$ | 0.0017 |
| **1c** | $1 \times 10^{-3}$ [$2 \times 10^5$] | $2 \times 10^{-4}$ | 0.0053 |

[1] Hole mobility ($\mu_h$) at the specified electric field. [2] Zero-field mobility ($\mu_0$). [3] Field dependence ($\alpha$). The measurements were performed under ambient conditions at room temperature. The layers were prepared under vacuum evaporation, with thicknesses ranging from 0.56 to 1.4 μm.

### 3.3. Organic Thin-Film Transistors

Considering the appropriate hole-transporting properties in conjunction with the adequate energy levels of compounds **1a–c**, all of them were tested as p-type semiconductors in OTFT. The characteristics of the OTFT devices fabricated from **1a–c** over OTS- and PS-treated $Si/SiO_2$ substrates are compiled in Table 4.

**Table 4.** OTFT characteristics of devices integrating compounds **1a–c** over $Si/SiO_2$ substrates passivated with either OTS or PS.

| Compound | $SiO_2$/OTS | | $SiO_2$/PS | |
|---|---|---|---|---|
| | $\mu_h$ ($cm^2$ $V^{-1}$ $s^{-1}$) | $I_{on}/I_{off}$ | $\mu_h$ ($cm^2$ $V^{-1}$ $s^{-1}$) | $I_{on}/I_{off}$ |
| **1a** | $7 \times 10^{-5}$ | $10^3$ | $6 \times 10^{-5}$ | $10^2$ |
| **1b** | $2 \times 10^{-4}$ | $10^4$ | $1 \times 10^{-4}$ | $10^3$ |
| **1c** | $5 \times 10^{-4}$ | $10^4$ | $2 \times 10^{-4}$ | $10^4$ |

As observed, the length of the *N*-alkyl chains appears as the main factor to modulate the hole mobility. In fact, the substitution of the *N*-methyl by the *N*-decyl implies an increase in the $\mu_h$ up to an order of magnitude over OTS-treated substrates, from $7 \times 10^{-5}$ to $5 \times 10^{-4}$ $cm^2$ $V^{-1}$ $s^{-1}$. The trend displayed by OTFT devices is, therefore, consistent with the results collected via TOF measurements. The effect of the *N*-alkylation on the performance of triindole also surpasses that of the nature of the aromatic moieties. Specifically, the attachment of alternative sulfurated scaffolds (i.e., 5-methylthien-2-yl and benzothien-2-yl) or aromatic hydrocarbons (i.e., phenyl and naphtyl) could only modulate the $\mu_h$ from $2 \times 10^{-4}$ to $4 \times 10^{-4}$ $cm^2$ $V^{-1}$ $s^{-1}$ [33]. The $I_{on}/I_{off}$ ratios follow the same tendency, with higher and more suitable values of ca. $10^4$ in the case of the *N*-decylated **1c**. Considering the effect of the passivation layer, OTS-containing devices slightly outperform their PS counterparts. This effect is also more significant with derivatives featuring longer *N*-alkyl chains. Another point to highlight is that devices fabricated with the *N*-methylated derivative **1a** display very linear saturation characteristics and low threshold voltage. Contrarily, derivatives **1b,c** exhibit a kink, so the charge mobility values were extracted from the region at higher $V_G$, as suggested in the literature [51,52]. The OTFT characteristics of devices fabricated from compounds **1a–c** over OTS-treated substrates are illustrated in Figure 3, whereas those of their PS counterparts can be found in the Supporting Information. The evolution of the hole mobility through time was also monitored to evaluate the air stability of this core, a feature that is highly coveted in organic electronics. As shown in Figure 3d, compounds **1a–c** exhibit minimal fluctuation of the hole mobility throughout a month. Their notorious air-stability was also corroborated by a shelf lifetime surpassing 100 days (Figure S7).

### 3.4. Solid-State Characterization

#### 3.4.1. Crystallographic Data

The crystal structure of derivative **1a** could be elucidated by means of single-crystal X-ray diffraction. The ORTEP projection and the molecular packing detailing the main intermolecular interactions are depicted in Figure 4. Compound **1a** crystallized in space group *P*–1 of the triclinic system, with dimensions $a$ = 7.2546 (7) Å, $b$ = 14.2460 (14) Å, $c$ = 14.4915 (15) Å, $\alpha$ = 95.662 (5)°, $\beta$ = 100.412 (4)°, and $\gamma$ = 98.766 (4)°, and a total volume of 1443.5(3) $Å^3$. The intermolecular packing could be classified as a β-type or sheet [53,54], featuring slightly displaced cofacial interactions. This type of arrangement is often considered as optimal for charge transport due to the strong π-overlap between molecules [54,55]. Specifically, the π–π interactions show conveniently short distances as close as 3.34 Å (Figure 4c). The methyl chains also assist and reinforce the packing with CH···π interactions. It should be noted that the triindole backbone is not entirely planar, since the peripheral benzene rings display a deviation of ca. 9° with respect to the central one. The thiophene moieties also show torsion angles with respect to the triindole nucleus

that go from 13.4 to 40.8° (Figure 4a). In spite of this, the arrangement of derivative **1a** is prone to facilitating the charge transport throughout the material.

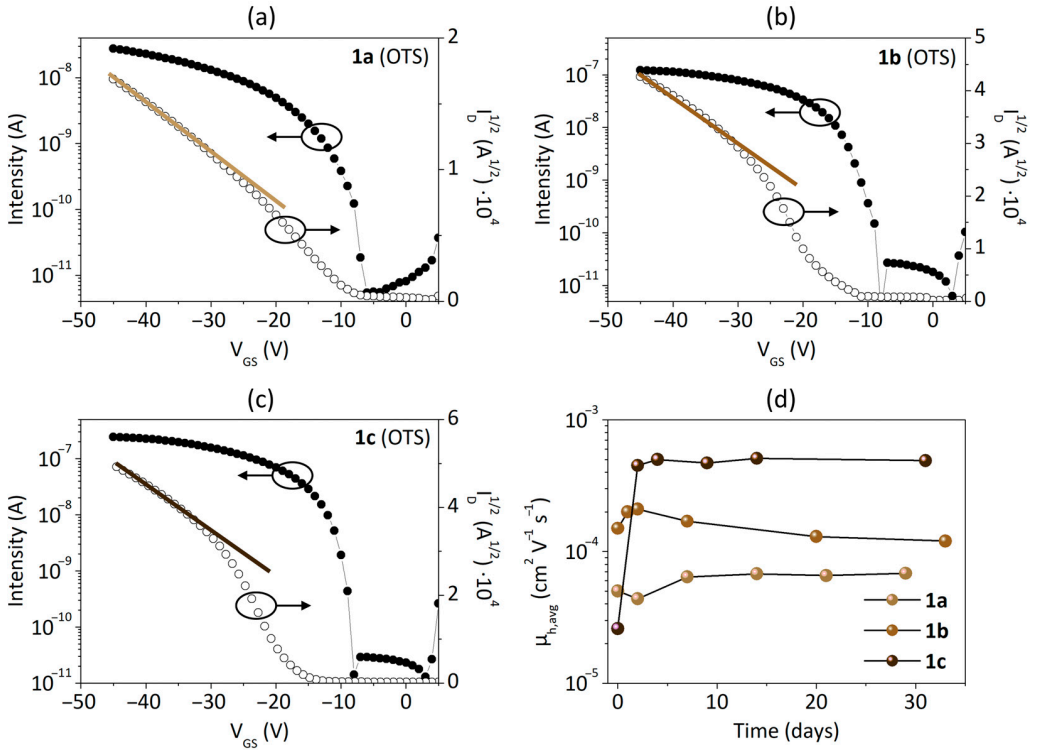


**Figure 3.** OTFT characteristics of OTS-functionalized devices based on compounds: (**a**) **1a**; (**b**) **1b**; (**c**) **1c**. The evolution of $\mu_h$ of representative devices throughout a month is represented in (**d**).

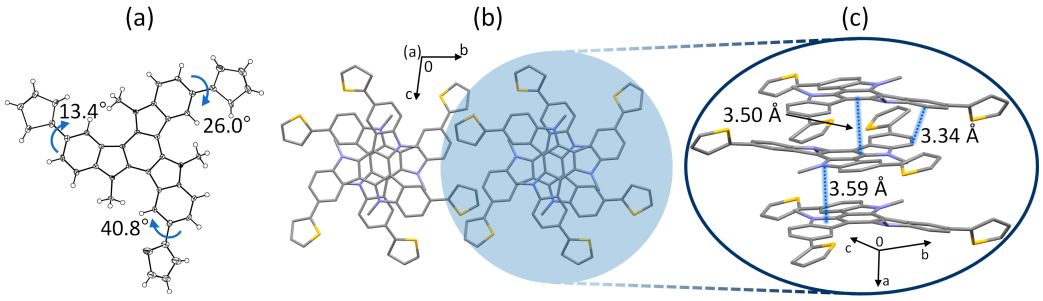


**Figure 4.** Crystal structure of derivative **1a**: (**a**) ORTEP projection, indicating the torsion angles between the triindole nucleus and the thiophene scaffolds; (**b**) intermolecular packing observed from the plane (100); (**c**) amplified region indicating the π-stacking distances.

### 3.4.2. Order and Morphology of the Thin Films

In order to correlate the characteristics of the OTFT devices based on derivatives **1a–c** with the analyzed structural variations, the crystallinity and disposition within the thin films was evaluated by means of grazing incidence X-ray diffraction (GIXRD). The GIXRD patterns, illustrated in Figure 5a,b, are consistent with the tendency exhibited by the OTFT devices. The longer the *N*-alkyl chains, the sharper and more intense the diffraction peaks, which indicates a more prominent degree of order and crystallinity in the thin films. Comparing the nature of the passivation layer, the outperforming OTS-treated devices also provide more crystalline films than their PS analogs in derivatives **1b,c**.

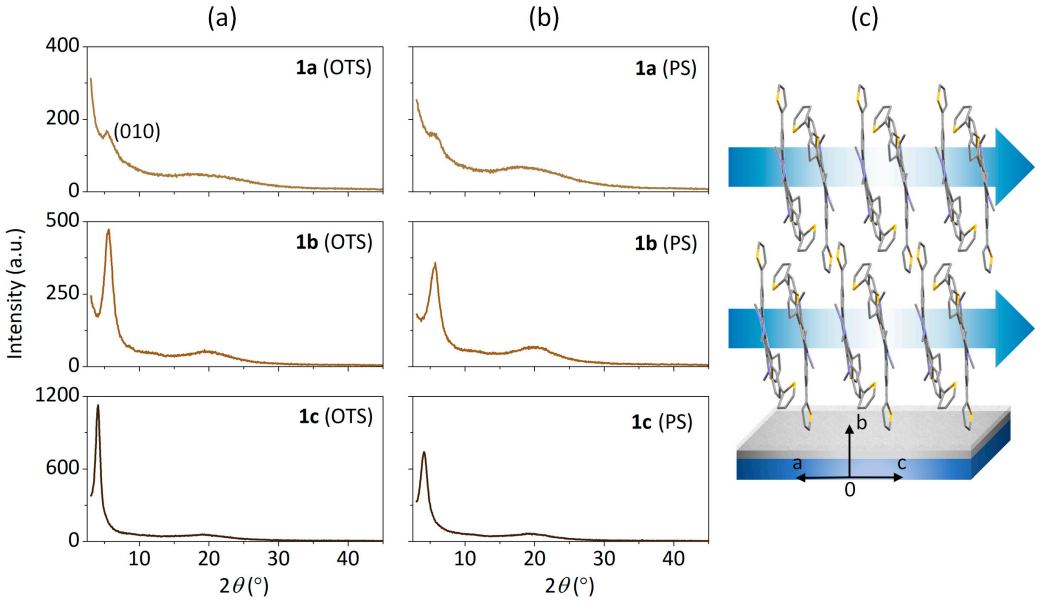


**Figure 5.** GIXRD patterns of thin films of **1a–c** deposited over $Si/SiO_2$ substrates passivated with OTS (**a**) and PS (**b**), and the proposed arrangement of **1a** over the substrate and the π-stacking direction (**c**), based on the GIXRD patterns and the elucidated single-crystal structure.

The *N*-methylated **1a** provides a rather amorphous arrangement regardless of the passivation layer, agreeing with the lower OTFT performance and the small difference between OTS and PS. Nevertheless, the availability of the single-crystal structure of **1a** permitted a closer insight into the arrangement of this material. From the simulated powder diffractogram, the diffraction signal peaking at $2\theta = 5.52°$ could be assigned as the plane (010), which stands parallel to the substrate. As represented in Figure 5c, the π-system of **1a** adopts a perpendicular disposition with respect to the substrate. Consequently, the π-stacking direction lays parallel to the substrate, ensuring a proper pathway for charge transport. The morphology of the vacuum-deposited thin films of **1a–c** over OTS- and PS-treated substrates was analyzed by means of atomic force microscopy (AFM). The AFM images, depicted in Figure 6, reveal quite homogeneous layers with small protrusions or hillocks.

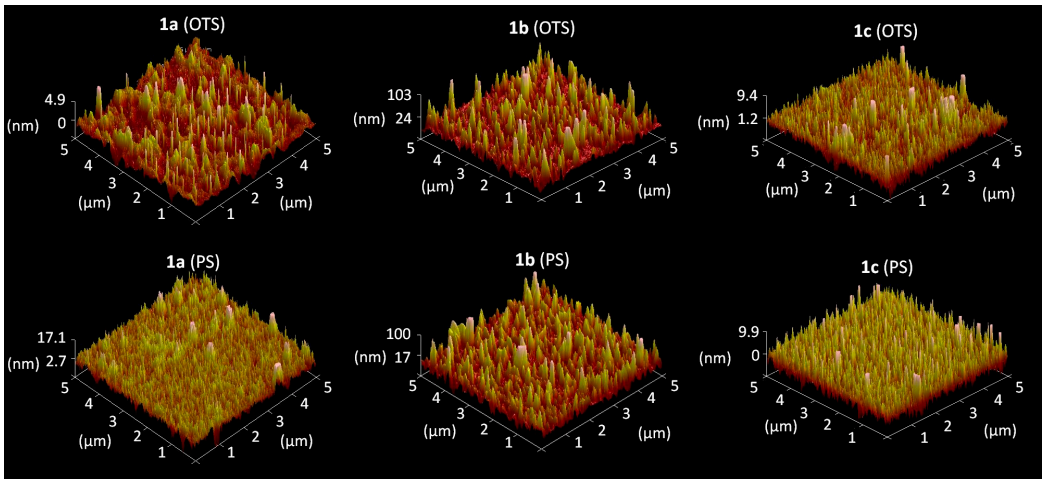


**Figure 6.** Morphology of the thin films based on compounds **1a–c** deposited over OTS (**above**) and PS (**below**).

The structural differences in derivatives **1a–c** are mainly translated into distinct grain sizes. The methylated derivative **1a** presents a quite uniform surface with undefined

domains of small grain sizes from 0.03 to 0.06 μm over PS, coinciding with the notoriously low degree of order detected via GIXRD. The deposition over OTS constitutes a more irregular layer but with slightly larger grains (0.1 μm). On the other hand, derivatives **1b**,**c** exhibit surface profiles with more defined regions and larger grain sizes from 0.15 to 0.3 μm over both OTS and PS, agreeing with the higher degree of order of the films. In addition, the minor roughness and morphology of **1c** films are again accordant to the superior hole mobilities extracted from the OTFTs.

## 4. Conclusions

Three thiophene-functionalized triindoles possessing different *N*-alkylation patterning (**1a–c**) were successfully synthesized in a facile four-step route. The incorporation of the thiophene moieties placed the ionization potential of the triindole nucleus at 5.11 eV in the solid state, making it perfectly suitable for hole injection while still preserving stability against oxidation. Particularly, the *N*-decylated derivative **1c** reached a hole mobility up to $1 \times 10^{-3}$ and $5 \times 10^{-4}$ $cm^2$ $V^{-1}$ $s^{-1}$ based on TOF and OTFT measurements, respectively. In fact, the presence of longer *N*-alkyl chains not only endowed the thin films with a higher degree of order and crystallinity, but also granted a more adequate morphology. The deposition of the thin film and its characteristics were also ameliorated by functionalizing the $Si/SiO_2$ surface with OTS in comparison with the PS coating. All these factors directly contributed to promoting the hole mobility in the respective OTFTs. Structurally, the strong π–π interactions and the favorable β packing found in the single crystal correlate with the good OTFT performance. Finally, the potential of these materials in organic electronics is supported by their outstanding air stability, which implies a minimal decrease in the OTFT performance and a shelf lifetime surpassing 100 days.

**Supplementary Materials:** The following Supporting Information can be downloaded at: https://www.mdpi.com/article/10.3390/coatings13050896/s1, Synthetic procedures and characterization; Figure S1: TGA scans of compounds **1a–c**. The decomposition temperatures ($T_d$) were estimated from the onset; Figure S2: Absorption and emission spectra of compounds **1a–c** in: (a) dichloromethane (10 μM) and (b) vacuum-evaporated thin films; Figure S3: Electrochemical data of compounds **1a–c**: (a) cyclic voltammogram of **1b** as representative (the inset shows the first oxidation step) and (b) photoemission spectra of compounds **1a–c**; Figure S4: Estimation of the hole mobility of compounds **1a–c** via the TOF technique: (a) TOF transients (the inset shows one of the transient curves in the linear plot) and (b) electric field dependence of the hole mobility; Figure S5: Output characteristics ($V_G$ from 0 to −40 V) of OTS-treated devices based on compounds: (a) **1a**; (b) **1a**; and (c) **1c**; Figure S6: OTFT characteristics of PS-treated devices incorporating derivatives **1a–c**: (a) transfer and saturation ($V_{DS}$ = −40 V) and (b) output characteristics; Figure S7: Transfer and saturation ($V_{DS}$ = −40 V) characteristics of devices fabricated with compound **1b** after 132 days (above) and **1c** after 122 days (below) over: (a) OTS- and (b) PS-treated substrates.

**Author Contributions:** Conceptualization, R.B., A.C. and D.V. (Dolores Velasco); validation, J.V.G., J.P. and D.V. (Dolores Velasco); formal analysis, R.B., A.C. and D.V. (Dmytro Volyniuk); investigation, R.B. and A.C.; resources, J.V.G., J.P. and D.V. (Dolores Velasco); data curation, R.B., A.C. and D.V. (Dmytro Volyniuk); writing—original draft preparation, R.B. and A.C.; writing—review and editing, R.B., J.V.G., J.P. and D.V. (Dolores Velasco); supervision, J.V.G., J.P. and D.V. (Dolores Velasco); project administration, D.V. (Dolores Velasco); funding acquisition, J.V.G., J.P. and D.V. (Dolores Velasco). All authors have read and agreed to the published version of the manuscript.

**Funding:** This research was funded by the Ministerio de Economía, Indústria y Competitividad, grant number FUNMAT-PGC2018-095477-B-I00, and the Ministerio de Ciencia e Innovación, grant number PID2020-116719RB-C41.

**Data Availability Statement:** Not applicable.

**Acknowledgments:** The authors want to thank Mercè Font-Bardía and Josep M. Bassas of the DRX unit of the CCiTUB for their assistance with the crystallographic elucidation and GIXRD measurements, respectively. Furthermore, thank you to Jordi Díaz of the CCiTUB for the assistance in AFM measures. R.B. and A.C. are thankful for the grant FI AGAUR from Generalitat de Catalunya.

**Conflicts of Interest:** The authors declare no conflict of interest.

## References


1. Wang, C.; Dong, H.; Jiang, L.; Huanli, D. Organic semiconductor crystals. *Chem. Soc. Rev.* **2017**, *47*, 422–500. [CrossRef] [PubMed]
2. Wu, F.; Liu, Y.; Zhang, J.; Duan, S.; Ji, D.; Yang, H. Recent advances in high-mobility and high-stretchability organic field-effect transistors: From materials, devices to applications. *Small Methods* **2021**, *5*, 2100676. [CrossRef]
3. Peng, H.; He, X.; Jiang, H. Greater than 10 $cm^2$ $V^{-1}$ $s^{-1}$: A breakthrough of organic semiconductors for field-effect transistors. *Infomat* **2021**, *3*, 613–630. [CrossRef]
4. Paterson, A.F.; Singh, S.; Fallon, K.J.; Hodsden, T.; Han, Y.; Schroeder, B.C.; Bronstein, H.; Heeney, M.; McCulloch, I.; Anthopoulos, T.D. Recent progress in high-mobility organic transistors: A reality check. *Adv. Mater.* **2018**, *30*, 1801079. [CrossRef]
5. Scaccabarozzi, A.D.; Basu, A.; Aniés, F.; Liu, J.; Zapata-Arteaga, O.; Warren, R.; Firdaus, Y.; Nugraha, M.I.; Lin, Y.; Campoy-Quiles, M.; et al. Doping approaches for organic semiconductors. *Chem. Rev.* **2021**, *122*, 4420–4492. [CrossRef]
6. Jiang, H.; Zhu, S.; Cui, Z.; Li, Z.; Liang, Y.; Zhu, J.; Hu, P.; Zhang, H.-L.; Hu, W. High-performance five-ring-fused organic semiconductors for field-effect transistors. *Chem. Soc. Rev.* **2022**, *51*, 3071–3122. [CrossRef] [PubMed]
7. Tahir, M.; Din, I.U.; Zeb, M.; Aziz, F.; Wahab, F.; Gul, Z.; Alamgeer; Sarker, M.R.; Ali, S.; Ali, S.H.M.; et al. Thin Films Characterization and Study of N749-Black Dye for Photovoltaic Applications. *Coatings* **2022**, *12*, 1163. [CrossRef]
8. Bronstein, H.; Nielsen, C.B.; Schroeder, B.C.; McCulloch, I. The role of chemical design in the performance of organic semiconductors. *Nat. Rev. Chem.* **2020**, *4*, 66–77. [CrossRef] [PubMed]
9. Ueberricke, L.; Mastalerz, M. Triptycene end-capping as strategy in materials chemistry to control crystal packing and increase solubility. *Chem. Rec.* **2021**, *21*, 558–573. [CrossRef] [PubMed]
10. Danac, R.; Leontie, L.; Carlescu, A.; Shova, S.; Tiron, V.; Rusu, G.G.; Iacomi, F.; Gurlui, S.; Șușu, O.; Rusu, G.I. Electric conduction mechanism of some heterocyclic compounds, 4,4′-bipyridine and indolizine derivatives in thin films. *Thin Solid Film.* **2016**, *612*, 216–222. [CrossRef]
11. Zhao, X.; Chaudhry, S.T.; Mei, J. Chapter Five—Heterocyclic Building Blocks for Organic Semiconductors. In *Heterocyclic Chemistry in the 21st Century: A Tribute to Alan Katritzky*; Advances in Heterocyclic, Chemistry; Scriven, E.F.V., Ramsden, C.A., Eds.; Academic Press: Cambridge, MA, USA, 2017; Volume 121, pp. 133–171. [CrossRef]
12. Takimiya, K.; Osaka, I.; Nakano, M. π-Building Blocks for Organic Electronics: Revaluation of "Inductive" and "Resonance" Effects of π-Electron Deficient Units. *Chem. Mater.* **2014**, *26*, 587–593. [CrossRef]
13. Salman, S.; Sallenave, X.; Bucinskas, A.; Volyniuk, D.; Bezvikonnyi, O.; Andruleviciene, V.; Grazulevicius, J.V.; Sini, G. Effect of methoxy-substitutions on the hole transport properties of carbazole-based compounds: Pros and cons. *J. Mater. Chem. C* **2021**, *9*, 9941–9951. [CrossRef]
14. Vegiraju, S.; Luo, X.-L.; Li, L.-H.; Afraj, S.N.; Lee, C.; Zheng, D.; Hsieh, H.-C.; Lin, C.-C.; Hong, S.-H.; Tsai, H.-C.; et al. Solution processable pseudo n-thienoacenes via intramolecular S···S lock for high performance organic field effect transistors. *Chem. Mater.* **2020**, *32*, 1422–1429. [CrossRef]
15. Kim, Y.; Wang, B.; Suo, J.; Jatautiene, E.; Simokaitiene, J.; Durgaryan, R.; Volyniuk, D.; Hagfeldt, A.; Sini, G.; Grazulevicius, J.V. Additives-free indolo[3,2-b]carbazolebased hole-transporting materials for perovskite solar cells with three yeses: Stability, efficiency, simplicity. *Nano Energy* **2022**, *101*, 107618. [CrossRef]
16. Lei, T.; Wang, J.-Y.; Pei, J. Roles of Flexible Chains in Organic Semiconducting Materials. *Chem. Mater.* **2014**, *26*, 594–603. [CrossRef]
17. Mišicák, R.; Novota, M.; Weis, M.; Cigáň, M.; Šiffalovič, P.; Nádaždy, P.; Kožíšek, J.; Kožíšková, J.; Pavúk, M.; Putala, M. Effect of alkyl side chains on properties and organic transistor performance of 2,6-bis(2,2′-bithiophen-5-yl)naphthalene. *Synth. Met.* **2017**, *233*, 1–14. [CrossRef]
18. Reig, M.; Bagdziunas, G.; Ramanavicius, A.; Puigdollers, J.; Velasco, D. Interface engineering and solid-state organization for triindole-based p-type organic thin-film transistors. *Phys. Chem. Chem. Phys.* **2018**, *20*, 17889–17898. [CrossRef]
19. Shaik, B.; Park, J.H.; An, T.K.; Noh, Y.R.; Yoon, S.B.; Park, C.E.; Yoon, Y.J.; Kim, Y.-H.; Lee, S.-G. Small asymmetric anthracene-thiophene compounds as organic thin-film transistors. *Tetrahedron* **2013**, *69*, 8191–8198. [CrossRef]
20. Shaik, B.; Han, J.-H.; Song, D.J.; Kang, H.-M.; Kim, Y.B.; Park, C.E.; Lee, S.-G. Synthesis of donor–acceptor copolymer using benzoselenadiazole as acceptor for OTFT. *RSC Adv.* **2016**, *6*, 4070–4076. [CrossRef]
21. Ong, B.S.; Wu, Y.W.; Li, Y. Organic Semiconductors Based on Polythiophene and Indolo[3,2-*b*]carbazole. In *Organic Electronics: Materials, Manufacturing and Applications*; Klauk, H., Ed.; WILEY-VCH: Weinheim, Germany, 2006; pp. 75–107. [CrossRef]
22. Wex, B.; Kaafarani, B.R. Perspective on carbazole-based organic compounds as emitters and hosts in TADF applications. *J. Mater. Chem. C* **2017**, *5*, 8622–8653. [CrossRef]
23. Grybauskaite-Kaminskiene, G.; Volyniuk, D.; Mimaite, V.; Bezvikonnyi, O.; Bucinskas, A.; Bagdziunas, G.; Grazulevicius, J.V. Aggregation-enhanced emission and thermally activated delayed fluorescence of derivatives of 9-phenyl-9*H*-carbazole: Effects of methoxy and tert- butyl substituents. *Chem. Eur. J.* **2018**, *24*, 9581–9591. [CrossRef]
24. Górski, K.; Mech-Piskorz, J.; Pietraszkiewicz, M. From truxenes to heterotruxenes: Playing with heteroatoms and the symmetry of molecules. *New J. Chem.* **2022**, *46*, 8939–8966. [CrossRef]
25. Li, X.-C.; Wang, C.-Y.; Lai, W.-Y.; Huangab, W. Triazatruxene-based materials for organic electronics and optoelectronics. *J. Mater. Chem. C* **2016**, *4*, 10574–10587. [CrossRef]

26. Qian, X.; Zhu, Y.-Z.; Song, J.; Gao, X.-P.; Zheng, J.-Y. New donor-π-acceptor type triazatruxene derivatives for highly efficient dye-sensitized solar cells. *Org. Lett.* **2013**, *15*, 6034–6037. [CrossRef] [PubMed]
27. Bulut, I.; Chávez, P.; Mirloup, A.; Huaulmé, Q.; Hébraud, A.; Heinrich, B.; Fall, S.; Méry, S.; Ziessel, R.; Heiser, T.; et al. Thiazole-based scaffolding for high performance solar cells. *J. Mater. Chem. C* **2016**, *4*, 4296–4303. [CrossRef]
28. Bura, T.; Leclerc, N.; Bechara, R.; Lévêque, P.; Heiser, T.; Ziessel, R. Triazatruxene-Diketopyrrolopyrrole Dumbbell-Shaped Molecules as Photoactive Electron Donor for High-Efficiency Solution Processed Organic Solar Cells. *Adv. Energy Mater.* **2013**, *3*, 1118–1124. [CrossRef]
29. Lai, W.-Y.; He, Q.-Y.; Zhu, R.; Chen, Q.-Q.; Huang, W. Kinked star-shaped fluorene/triazatruxene co-oligomer hybrids with enhanced functional properties for high performance, solution-processed, blue organic light-emitting diodes. *Adv. Funct. Mater.* **2008**, *18*, 265–276. [CrossRef]
30. Chen, Y.; Wang, S.; Wu, X.; Xu, Y.; Li, H.; Liu, Y.; Tong, H.; Wang, L. Triazatruxene-based small molecules with thermally activated delayed fluorescence, aggregation-induced emission and mechanochromic luminescence properties for solution-processable nondoped OLEDs. *J. Mater. Chem. C* **2018**, *6*, 12503–12508. [CrossRef]
31. Hu, Y.-C.; Lin, Z.-L.; Huang, T.-C.; Lee, J.-W.; Wei, W.-C.; Ko, T.-Y.; Lo, C.-Y.; Chen, D.-G.; Chou, P.-T.; Hung, W.-Y.; et al. New exciplex systems composed of triazatruxene donors and *N*-heteroarene-cored acceptors. *Mater. Chem. Front.* **2020**, *4*, 2029–2039. [CrossRef]
32. Ruiz, C.; Arrechea-Marcos, I.; Benito-Hernández, A.; Gutierrez-Puebla, E.; Monge, M.A.; Navarrete, J.L.; Ruiz Delgado, M.C.; Ponce Ortiz, R.; Gómez-Lor, B. Solution-processed *N*-trialkylated triindoles for organic field effect transistors. *J. Mater. Chem. C* **2018**, *6*, 50–56. [CrossRef]
33. Cuadrado, A.; Cuesta, J.; Puigdollers, J.; Velasco, D. Air stable organic semiconductors based on diindolo[3,2-a:3′,2′-c]carbazole. *Org. Electron.* **2018**, *62*, 35–42. [CrossRef]
34. Reig, M.; Puigdollers, J.; Velasco, D. Molecular order of air-stable p-type organic thin-film transistors by tuning the extension of the π-conjugated core: The cases of indolo[3,2-*b*]carbazole and triindole semiconductors. *J. Mater. Chem. C* **2015**, *3*, 506–513. [CrossRef]
35. Takimiya, K.; Shinamura, S.; Osaka, I.; Miyazaki, E. Thienoacene-Based Organic Semiconductors. *Adv. Mater.* **2011**, *23*, 4347–4370. [CrossRef] [PubMed]
36. Ryu, S.; Yun, C.; Ryu, S.; Ahn, J.; Kim, C.; Seo, S. Characterization of [1]Benzothieno[3,2-*b*]benzothiophene (BTBT) Derivatives with End-Capping Groups as Solution-Processable Organic Semiconductors for Organic Field-Effect Transistors. *Coatings* **2023**, *13*, 181. [CrossRef]
37. Bujaldón, R.; Puigdollers, J.; Velasco, D. Towards the Bisbenzothienocarbazole Core: A Route of Sulfurated Carbazole Derivatives with Assorted Optoelectronic Properties and Applications. *Materials* **2021**, *14*, 3487. [CrossRef] [PubMed]
38. Borchert, J.W.; Peng, B.; Letzkus, F.; Burghartz, J.N.; Chan, P.K.L.; Zojer, K.; Ludwigs, S.; Klauk, H. Small contact resistance and high-frequency operation of flexible low-voltage inverted coplanar organic transistors. *Nat. Commun.* **2019**, *10*, 1119. [CrossRef]
39. Choi, E.; Jang, Y.; Ho, D.; Chae, W.; Earmme, T.; Kim, C.; Seo, S. Development of Dithieno[3,2-*b*:2′,3′-*d*]thiophene (DTT) Derivatives as Solution-Processable Small Molecular Semiconductors for Organic Thin Film Transistors. *Coatings* **2021**, *11*, 1222. [CrossRef]
40. Sugiyama, M.; Jancke, J.; Uemura, T.; Kondo, M.; Inoue, Y.; Namba, N.; Araki, T.; Fukushima, T.; Sekitani, T. Mobility enhancement of DNTT and BTBT derivative organic thin-film transistors by triptycene molecule modification. *Org. Electron.* **2021**, *96*, 106219. [CrossRef]
41. Singh, M.; Kaur, N.; Comini, E. The role of self-assembled monolayers in electronic devices. *J. Mater. Chem. C* **2020**, *8*, 3938–3955. [CrossRef]
42. Hasan, M.M.; Islam, M.M.; Li, X.; He, M.; Manley, R.; Chang, J.; Zhelev, N.; Mehrotra, K.; Jang, J. Interface Engineering with Polystyrene for High-Performance, Low-Voltage Driven Organic Thin Film Transistor. *IEEE Trans. Electron Devices* **2020**, *67*, 1751–1756. [CrossRef]
43. Kim, D.; Kim, C.A. Ladder-Type Organosilicate Copolymer Gate Dielectric Materials for Organic Thin-Film Transistors. *Coatings* **2018**, *8*, 236. [CrossRef]
44. Feriancová, L.; Kmentová, I.; Micjan, M.; Pavúk, M.; Weis, M.; Putala, M. Synthesis and Effect of the Structure of Bithienyl-Terminated Surfactants for Dielectric Layer Modification in Organic Transistor. *Materials* **2021**, *14*, 6345. [CrossRef] [PubMed]
45. Sun, H.; Liao, J.; Hou, S. Single-Molecule Field-Effect Transistors with Graphene Electrodes and Covalent Pyrazine Linkers. *Acta Phys. Chim. Sin.* **2021**, *37*, 1906027. [CrossRef]
46. Demas, J.N.; Crosby, G.A. Measurement of photoluminescence quantum yields. Review. *J. Phys. Chem.* **1971**, *75*, 991–1024. [CrossRef]
47. Cardona, C.M.; Li, W.; Kaifer, A.E.; Stockdale, D.; Bazan, G.C. Electrochemical considerations for determining absolute frontier orbital energy levels of conjugated polymers for solar cell applications. *Adv. Mater.* **2011**, *23*, 2367–2371. [CrossRef]
48. Ghalgaoui, A.; Shimizu, R.; Hosseinpour, S.; Álvarez-Asencio, R.; McKee, C.; Johnson, C.M.; Rutland, M.W. Monolayer Study by VSFS: In Situ Response to Compression and Shear in a Contact. *Langmuir* **2014**, *30*, 3075–3085. [CrossRef]
49. Song, D.; Wang, H.; Zhu, F.; Yang, J.; Tian, H.; Geng, Y.; Yan, D. Phthalocyanato Tin(IV) Dichloride: An Air-Stable, High-Performance, n-Type Organic Semiconductorwith a High Field-Effect Electron Mobility. *Adv. Mater.* **2008**, *20*, 2142–2144. [CrossRef]

50. Miyaura, N.; Suzuki, A. Palladium-Catalyzed Cross-Coupling Reactions of Organoboron Compounds. *Chem. Rev.* **1995**, *95*, 2457–2483. [CrossRef]
51. McCulloch, I.; Salleo, A.; Chabinyc, M. Avoid the kinks when measuring mobility. *Science* **2016**, *352*, 1521–1522. [CrossRef] [PubMed]
52. Choi, H.H.; Cho, K.; Frisbie, C.D.; Sirringhaus, H.; Podzorov, V. Critical assessment of charge mobility extraction in FETs. *Nat. Mater.* **2018**, *17*, 2–7. [CrossRef] [PubMed]
53. Desiraju, G.R.; Gavezzotti, A. Crystal structures of polynuclear aromatic hydrocarbons. Classification, rationalization and prediction from molecular structure. *Acta Cryst.* **1989**, *45*, 473–482. [CrossRef]
54. Campbell, J.E.; Yang, J.; Day, G.M. Predicted energy–structure–function maps for the evaluation of small molecule organic semiconductors. *J. Mater. Chem. C* **2017**, *5*, 7574–7584. [CrossRef]
55. Mas-Torrent, M.; Rovira, C. Role of Molecular Order and Solid-State Structure in Organic Field-Effect Transistors. *Chem. Rev.* **2011**, *111*, 4833–4856. [CrossRef] [PubMed]